Chapter 2
The Hydrogen Evolution Reaction: Water Reduction Photocatalysis—Improved Niobate Nanoscroll Photocatalysts for Partial Water Splitting

2.1 Introduction

Development of a photocatalyst for harvesting the practically endless sources of fuel from sunlight and water may be one of the most important challenges of the century. Semiconductor photocatalysts are expected to be the most promising solution to the global energy dilemma [1]. However, due to low efficiencies ($\eta < 10$ %) of solar to hydrogen conversion and limited light absorption, no economically competitive water splitting photocatalyst has yet been realized. Compared to the traditionally large catalysts (>1 μm), nanomaterials offer potential advantages due to their higher catalytic surface areas and shorter semiconductor-liquid electron pathways for charge and exciton transport. For example, Bulk Fe_2O_3, which is known to suffer from high recombination rates and short diffusion lengths was made active as a photoanode nanomaterial [2]. In addition to enhanced surface areas, nanoscale semiconductors also exhibit quantum confinement effects which can be used to adjust energy levels and light absorption. This phenomenon allowed for non-active bulk-CdSe to be activated on the nanoscale because of the raising of the conduction band above the electrochemical reduction potential for water [3, 4]. One problem with nanostructures that needs to be addressed is that the space charge regions, if present at all, are not strong enough to enable efficient electron hole separation. The attachment of cocatalysts could potentially solve this issue since they can act as selective electron hole acceptors. However, data on the energetic structures of these nanomaterials and composites are still scarce, so optimization of such contacts presents a challenge. In addition, there are also synthetic obstacles for the preparation of well-defined multi-component nanostructures. As part of our ongoing search for a nanoscale water splitting photocatalyst [3–12], we describe here scalable syntheses of catalysts that contain up to three separate nanoparticle components for light absorption, water reduction and oxidation. For this investigation, we used a nanoscale derivative of

This chapter appeared as: "T.-K. Townsend, et al., *Improved Niobate Nanoscroll Photocatalysts for Partial Water Splitting*, Chem. Sus. Chem. **4**(2), 185–190 (2011)."

© Springer International Publishing Switzerland 2014

$K_4Nb_6O_{17}$ which is known to exfoliate into an asymmetrical scroll structure as the light absorbing material [13–16]. Charge separation on this material is thought to also be asymmetric due to the nature of the unique crystal orientations of the scroll framework. In order to introduce electronically separated sites for water reduction and oxidation, Pt and IrOx (x = 1.5–2) nanoparticle cocatalysts are attached to the nanoscrolls via photochemical deposition, respectively. The morphology, optical, electrochemical, photocatalytic and energetic properties of these nanomaterials are also investigated.

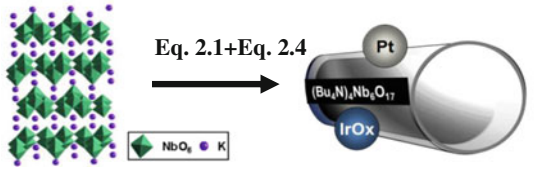
2.2 Results and Discussion

The formation of niobate nanoscrolls and the incorporation of the Pt and IrOx cocatalysts are shown in Scheme 2.1 (Eqs. 2.1–2.4). After the solid state synthesis of bulk $K_4Nb_6O_{17}$ crystals, dilute acid and tetrabutylammonium hydroxide addition leads to the exfoliation of the crystal into individual nanosheets. These naturally turn into scrolls **[1]** because of the inherent strain of the asymmetrical structure [16]. When **[1]** are irradiated in the presence of potassium hexachloroiridate (III) and nitrate as electron acceptor, one obtains the scrolls modified with IrOx cocatalyst **[2]** (Scheme 2.1, Eq. 2.2). Scrolls decorated with platinum nanoparticles (Scheme 2.1, Eq. 2.3) can be produced via photochemical reduction of hexachloroplatinic acid and methanol as an electron donor **[3]**. By combining these two cocatalyst depositions (Scheme 2.1, Eq. 2.4), three-component nanocatalysts were produced **[4]** by either sequential deposition of first Pt and then IrOx, or by co-deposition in a one-pot deposition. Products of these aqueous processes were precipitated and cleaned as described in the experimental section.

$$K_4Nb_6O_{17(s)} + 4HNO_{3(aq)} + 4(Bu_4N)OH_{(aq)} \overset{5\ days}{\rightarrow} (\mathbf{Bu_4N})_4\mathbf{Nb_6O_{17(s)}}[1] + 4KNO_3 + 4H_2O \tag{2.1}$$

$$(Bu_4N)_4Nb_6O_{17(s)} + K_3IrCl_6 + {}^1\!/_2KNO_3 + 3OH^- \overset{hv}{\rightarrow} [1\mathbf{wt.\%}\ \boldsymbol{IrO_2}](\boldsymbol{Bu_4N})_4\boldsymbol{Nb_6O_{17}}[2] + {}^1\!/_2KNO_2 + {}^3\!/_2H_2O + 3K^+ + 6Cl^- \tag{2.2}$$

$$(Bu_4N)_4Nb_6O_{17(s)} + H_2PtCl_6.6H_2O + 6OH^- \overset{hv}{\rightarrow} [1\mathbf{wt.\%}\ \boldsymbol{Pt}](\boldsymbol{Bu_4N})_4\boldsymbol{Nb_6O_{17}}\ [3] + O_2 + 6Cl^- + 10H_2O \tag{2.3}$$



$$[4], wt\% = \frac{mass\ Pt\ or\ IrO_2}{mass\ Bu_4N_4Nb_6O_{17}} \times 100$$

Scheme 2.1 Synthesis of nanocrystal photocatalysts (Eqs. 2.1–2.4). The structure of $K_4Nb_6O_{17}$ (including exfoliation *lines*) and the schematic structure of the nanoscrolls with co-catalysts are also shown where wt.% cocatalyst loading is defined

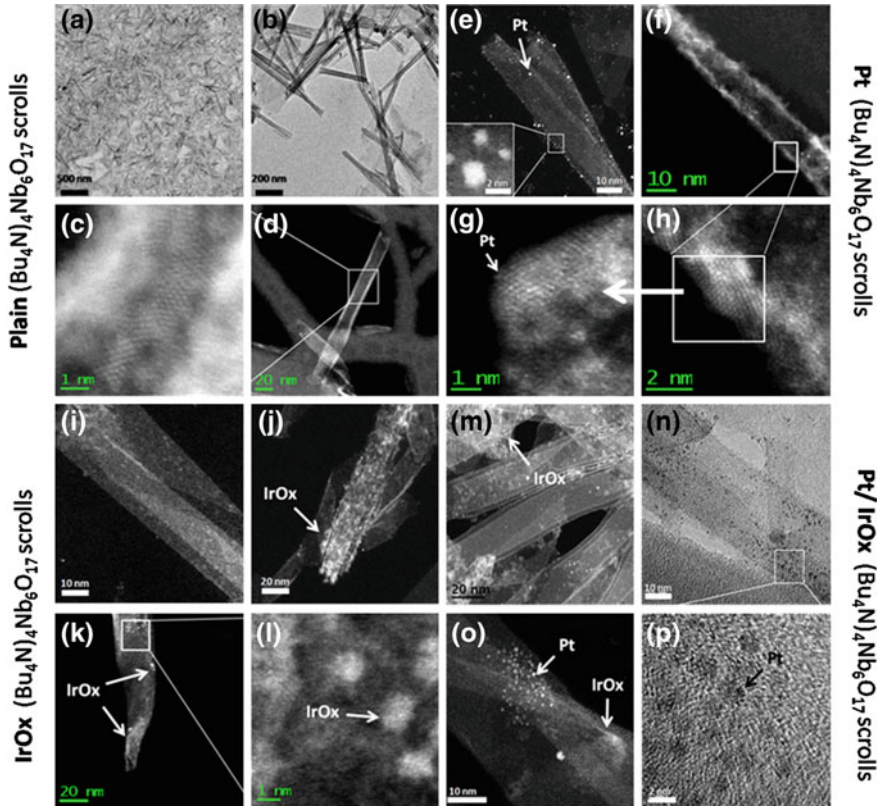


Fig. 2.1 TEM (**a**, **b**), High Angle Annular Dark Field (HAADFSTEM) (**c**–**m**, **o**), and HRTEM (**n**, **p**) of $(Bu_4N)_4\ Nb_6O_{17}$ nanoscroll (**a**–**d**), Pt nanoscroll (**e**–**h**), IrOx nanoscroll (**i**–**l**), and Pt/IrOx nanoscroll (**m**–**p**)

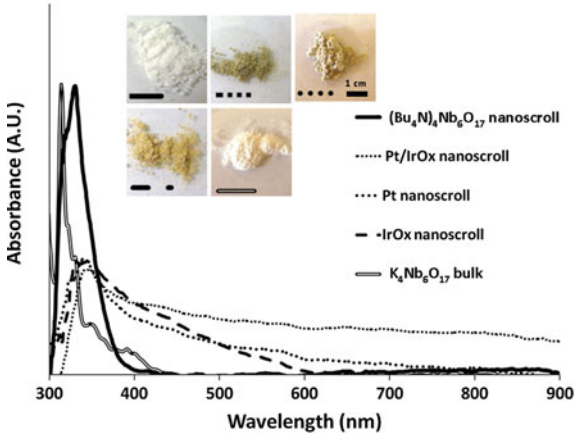


Fig. 2.2 Diffuse reflectance UV/Vis spectra of four catalysts and the parent material ($K_4Nb_6O_{17}$) with photographs showing coloration due to cocatalyst deposition

$$(Bu_4N)_4Nb_6O_{17(s)} + K_3IrCl_6 + H_2PtCl_6.6H_2O + 1/2KNO_3 + 9OH^- \xrightarrow{hv} [\boldsymbol{0.5wt.\%IrO_2|0.5wt.\%Pt}](\boldsymbol{Bu_4N})_4\boldsymbol{Nb_6O_{17}}[\boldsymbol{14}] + 1/2KNO_2 + 3K^+ + 11.5H_2O + O_2 + 12Cl^- \quad (2.4)$$

Transmission electron microscopy (TEM) was used to confirm the morphologies of the products **1–4**. The niobate scroll platform [**1**] are 1 ± 0.5 μm long and 10 ± 5 nm wide (Fig. 2.1a, b), in agreement with observations by Saupe et al. [16]. Characteristic spacing between rows of Nb atoms in the overlapping lattice fringes are evident in Fig. 2.1c, d [17, 18]. The surfaces of [**3**] show nanocrystals of Pt^0 metal (<2 nm) discretely deposited on the surface (Fig. 2.1e–h). When imaged with High Resolution Scanning Transmission Electron Microscopy (HRSTEM), the lattice fringes of the crystalline Pt particles were measured as 0.195 nm and match the known spacing of platinum for the [100] axis [19]. In contrast, the 1 wt.% IrO_x nanoscrolls in Fig. 2.1i–l showed no visible lattice fringes indicating an amorphous deposition. IrO_x is known to form an amorphous oxide/hydroxide phase when grown in solution phase [20]. The three-component catalysts containing 0.5 wt.% Pt and 0.5 wt.% IrOx share features displayed in both of the two-component structures. Pt and IrOx (Fig. 2.1m–p). These two cocatalysts could also be directly identified and mapped with Energy Dispersive Spectroscopy (EDS, see Fig. 2.7 in Supporting Information). While IrOx deposition appeared to have no selectivity, regioselective deposition of Pt onto the asymmetric nanoscroll was observed with Pt growing predominately on the edges of the rolled crystal sheets.

The optical absorption edge of $K_4Nb_6O_{17}$ (348 nm) corresponds to the 3.55 eV band gap of the parent material is shown in the UV-Vis spectra (Fig. 2.2). The nanoscale version of this material [**1**] has a red-shifted absorption onset (to 375 nm) corresponding to a reduced band gap of 3.3 eV which we have previously attributed to Nb–O bond weakening as a result of strain induced from bending of

Table 2.1 Catalyst turnover numbers calculated as moles of formed H_2/O_2 per mole of $H_4Nb_6O_{17}$ catalyst (MW = 834 g/mol, 120 μ mol for 100 mg) after a 5 h irradiation

	Catalyst	Solution		
	$H_4Nb_6O_{17}$ nanoscroll	Pure water	20 % (vol) methanol	25 mM $AgNo_3$
(1)	Unmodified	2.3	4.9	0.1
(2)	IrOx	8.3	6.24	0.1
(3)	Pt	8.3	18.5	0.0
(4)	Pt/IrOx	4.6	14.4	0.1

the crystal plane [9]. After cocatalyst deposition, the materials become colored (see photographs in Fig. 2.2) due to the visible absorption of Pt and IrOx. The Pt coated scrolls appear brown due to broad visible absorption similar to that of Pt colloids [21]. The IrO_x coated scrolls are also brown, not blue as observed for colloidal Ir(IV)O_2 [22]. The brown color indicates the presence of Ir^{3+} oxidation state which may not be as active as Ir^{4+}; however, Ir(III)oxide is also known to be an active water oxidation catalyst [23, 24]. The three component samples share optical characteristics with both two-component catalysts.

Photo-irradiation experiments with the nanoscroll catalysts were conducted over 5 h periods in aqueous methanol (20 % vol), 25 mM aqueous silver nitrate solution, and in pure water, using 100 mg (∼55.6 μ mol) of catalyst in each case. From methanol solution, all catalysts evolve H_2 at a constant rate. [Pt] $(Bu_4N)_4$ Nb_6O_{17} **[3]** is most active (∼500 μ mol/h), followed by [IrOx, Pt] $(Bu_4N)_4$ Nb_6O_{17} **(4,** ∼250 μmol/h), $(Bu_4N)_4$ Nb_6O_{17} **[1]**, and [IrOx] $(Bu_4N)_4$ Nb_6O_{17} **[2]** the latter of which evolve H_2 at nearly the same rate of ∼100 μmol/h. Turnover numbers range between 10.6 (for **1**) to 40 (for **3**), establishing a catalytic process (Table 2.1).

Each catalyst **[1–4]** evolve H_2 from pure water in the presence of light, but the rates are only about half of that in aqueous methanol. As expected, **[2]** shows the lowest activity in methanol and the relative activities of the four catalysts remain unchanged whether in aqueous methanol or in water. Importantly, we find that in water, H_2 evolution cannot be sustained and in the case of the most active **[3]** drops to nearly zero after 24 h of continuous irradiation (Fig. 2.3d). We have previously attributed this to the formation of surface peroxides which terminate the oxygen formation reaction and inhibit the active sites for water reduction as seen with the related phase $HCa_2Nb_3O_{10}$ [8]. The formation of hydrogen and Nb (5 +)-bound μ^2-peroxide is favored over the more demanding water oxidation steps. To investigate this further, titration of pre-irradiated platinated scrolls **[3]** was performed with o-Tolidine indicator (details in supporting information) revealing that peroxides are also present in 1:1 stoichiometry with regard to the amount of gaseous H_2 released (Fig. 2.3d) confirming the surface passivation of the catalysts with peroxides. After replacement of residual tetrabutylammonium (TBA) surfactant with protons via repeated precipitation/washing steps, the $H_4Nb_6O_{17}$ scrolls (100 mg) evolve up to 680 μmol of H_2 over a 24 h period, i.e. H_2:$H_4Nb_6O_{17}$ = 5.7. This number

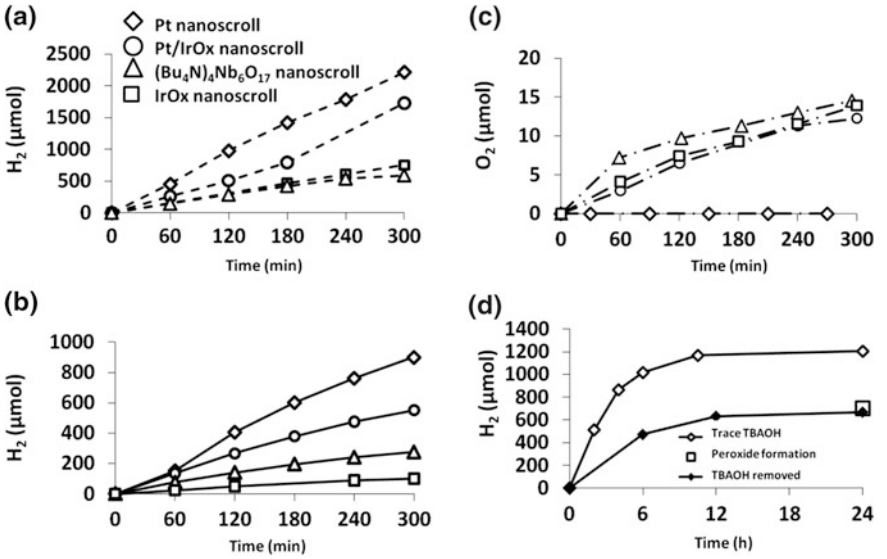


Fig. 2.3 H_2 and O_2 evolution under UV-light irradiation with a 300 W Xe arc lamp from 100 mg of catalysts suspended in 50 mL of 20 % aqueous methanol (**a**– –), pure water (**b**—), and 25 mM aqueous $AgNO_3$ (**c**–·–). (D). Hydrogen evolution during long term (24 h) irradiation of 100 mg 1 %Pt nanoscrolls (3) in water. Also shown in the plot is H_2 evolution data for 3 after removal of residual tetrabutyl ammonium hydroxide (TBAOH), and the amount of peroxide detected coulometrically via reaction with o-tolidine (for details see Fig. 2.8 in Supporting Information)

agrees very well with our experimental data assuming that each of the six niobium ions in the scrolls can accommodate one peroxide ligand, the scrolls can release at most six mole equivalents of hydrogen. In the presence of TBA, the amount of H_2 from irradiation in water is higher (see Fig. 2.4d and first column in Table 2.1). We attribute this to side reactions of the peroxide with the tetrabutylammonium ion, as previously described for TBA $Ca_2Nb_3O_{10}$ nanosheets [8].

In contrast to H_2 evolution, water oxidation to promote O_2 evolution is a multistep process involving high energy intermediates. As a result, peroxide intermediate products are formed without further reaction. This leads to difficulty of the photocatalysts to release O_2 from water and even from sacrificial solution of aqueous $AgNO_3$ (Fig. 2.3). The O_2 evolution rate declines over time, in part due to peroxide poisoning of the catalyst, and also as a result of Ag particle deposition onto the scrolls. Only non-catalytic amounts of O_2 are formed, or none as in the case of [Pt] $(Bu_4N)_4$ Nb_6O_{17}.

Cyclic voltammetry was used to gain further insight into the reasons for varying catalytic activities of these nanocomposites (Fig. 2.4). Electrochemically, water oxidation is observed for all materials significantly above the theoretical potential (+820 mV vs. NHE at pH 7). The first oxidation wave at +1.10 belongs to the two-electron oxidation of water to peroxide as shown in Fig. 2.5, with a corresponding

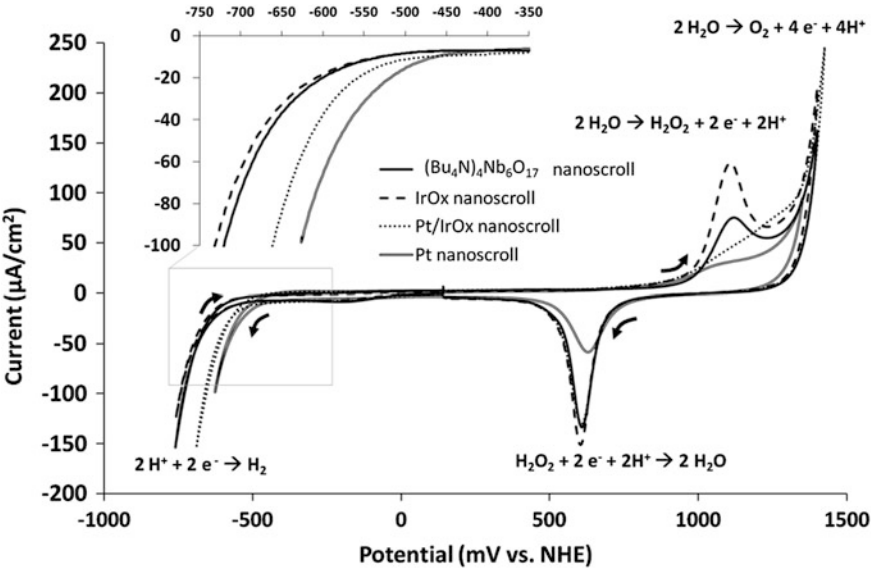


Fig. 2.4 Cyclic voltammograms of films of the four catalysts on a Au electrode (1 cm^2) in 0.25 M NaH_2PO_4/Na_2HPO_4 buffer at pH 7 and scan rate of 10 mV/s. *Arrows* show scan direction. All potentials are given versus NHE. Additional scans on bare Pt and Au electrodes (Fig. 2.9 in supporting information) show that background currents from the Au electrode can be neglected

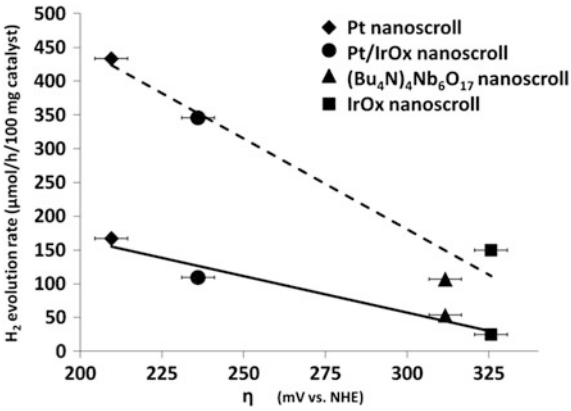


Fig. 2.5 Correlation between measured reduction overpotentials and photocatalytic H_2 evolution rate from 20 % (vol) aqueous methanol (– –) and pure water (—). Error bars correspond to 10 % experimental error

reduction process on the reverse scan occurring at +600 mV. The shapes and potentials of these redox features are very similar to gold electrodes, after correcting for the difference in pH [25, 26]. Indeed, if the nanoscroll film is kept at 1.2 V NHE bias for 1 h, peroxides can be directly detected on the surface using a peroxidase-coated test strip (Fig. 2.10). Peroxide formation is favored energetically because of the strong binding affinity to Nb (5+) and kinetically, because it

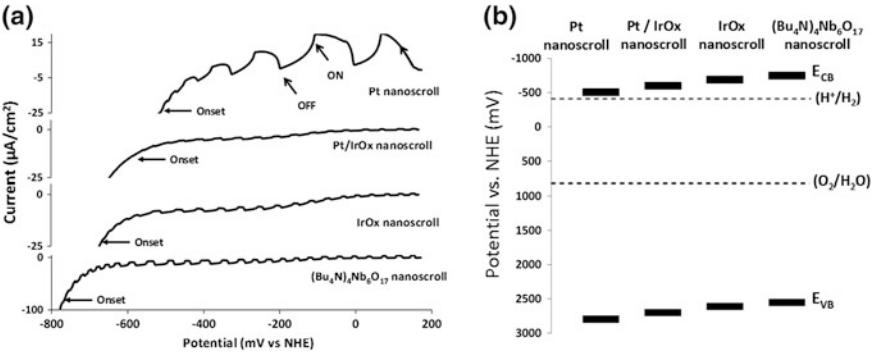


Fig. 2.6 Reduction scans (10 mV/s) of catalysts deposited and dried as a thin film onto a gold 1 cm^2 electrode in 25 mM NaH_2PO_4 pH 7 buffer with chopped light (**a**) and resulting energy band diagrams of each catalyst (**b**)

involves fewer redox steps and fewer reactive intermediates in comparison to O_2 formation.

Cathodic scans reveal significant differences of 0.21–0.325 V between the actual and theoretical reduction potential for water (−410 mV vs. NHE at pH 7). The scrolls containing 1 % Pt cocatalysts [**3**] showed the lowest reduction overpotential (0.21 V), as would be expected from the high catalytic conversions. For the other catalysts, cathodic overpotentials increase in the order Pt/IrOx [**4**] > nanoscroll [**1**] > IrOx [**2**]. This parallels the order of H_2 evolution activity for both water and aqueous methanol reactions. When plotted against the electrochemical overpotentials, the rates of H_2 evolution can be seen to fit a straight line in both cases, although the slope is greater in the presence of methanol (Fig. 2.5). This is expected because methanol acts as an electron donor since methanol oxidation is more favorable than water oxidation, so the proton reduction rate becomes the limiting factor. In pure water, the water oxidation reaction becomes rate limiting, based on the lower H_2 evolution rates from water in Fig. 2.2.

Water oxidation to form peroxide intermediates is observed as a peak for [**1**] and [**2**] and as a shoulder for the Pt containing materials, which could indicate a fast subsequent oxidation reaction (i.e. Pt—catalyzed peroxide disproportionation into H_2O and O_2. Based on the observation of residual peroxide reduction at +600 mV on the reverse scan, the consumption of peroxides is also incomplete for these catalysts as well, albeit lower amplitude for [**3**] with the most Pt loading. On the other hand, IrOx loaded scrolls are nearly identical to the bare scrolls which indicates that water oxidation proceeds mainly on the surface of the niobate rather than the IrOx sites as proposed.

Gas bubbles were observed evolving from the surface of the electrode as the voltage scan reached >1400 mV, corresponding to the formation of O_2. This is roughly the same for each catalyst, indicating that IrOx assumes a spectator role, and that the water oxidation reaction occurs on the surface of the niobate. This could be due to a few factors including the low mass fraction of the IrOx in [**2**] and

that there does not appear to be an efficient pathway for hole transport from the Nb–O sites to the IrOx particles. Also the amorphous IrOx may be less active for water oxidation in the +3 state versus the blue IrO_2 [23, 24]. Given that the water oxidation overpotential ($\sim$600 mV) is two–three times larger than the proton reduction overpotential (210–325 mV), it is clearly the oxygen evolution reaction that is the limiting factor in the photocatalytic water splitting activities of these materials. Since the Ag ion reduction potential of +0.8 V [27] is simply not sufficient to promote O_2 evolution from the scrolls, this also explains the low efficiency of O_2 evolution in the presence of silver nitrate.

Chopped light voltammetry experiments were also performed in the presence of methanol as an electron donor (Fig. 2.6a) in order to determine the onset potentials and the magnitude of the photocurrents. Each catalyst responds to illumination with a positive photocurrent, and the onset of this can be used to estimate the conduction band edge in highly n-doped semiconductors [28–30]. Onset potentials are observed from -0.50 to -0.80 V at pH $= 7$, and the sizes of the photocurrents differ among catalysts with the strongest currents observed with [Pt] $(Bu_4N)_4$ Nb_6O_{17} **[3]**. Together with the optical band gaps, this data was used to construct the energy diagrams in Fig. 2.6b. Based on this information, we can see that the conduction band energies of each catalyst are above the theoretical proton reduction potential in neutral solution (–410 mV vs. NHE) and therefore active for H_2 production. The addition of cocatalysts was found to depress the conduction band edge by 58 mV (IrOx), 148 mV (Pt/IrOx), and 242 mV (Pt) in positive direction from the value for the unmodified scrolls (-748 mV). We observed similar results with Pt-modified $H_2Ti_4O_9$ nanocrystals [12] and this can be interpreted as a result of electron transfer from the niobate to the cocatalysts in the direction of lower Fermi energy.

Due to the enormous interfacial area of the nanoscrolls and the cocatalyst particles, this phenomenon is more pronounced than would be expected for bulk materials. One might expect that the associated polarization should lessen the thermodynamic driving force for water reduction, thereby reducing the H_2 evolution rate. However, the opposite is observed here, because the photocatalytic H_2 activity in methanol solution is not controlled by the energetics of the catalysts but by the kinetics of proton reduction (electrochemical overpotentials). For water oxidation the situation is similar. Even though the valence band edges of all catalysts are well below the water oxidation potential, oxygen formation is inhibited kinetically due to the large overpotential for its formation and to the greater ease of peroxide formation on the niobate surface.

2.3 Conclusion

We have synthesized two- and three-component photocatalysts by a combination of top-down (exfoliation from bulk) and bottom-up approaches (photochemical deposition). The resulting Pt- and/or IrOx coated niobate nanoscrolls evolve

catalytic amounts of H_2 from aqueous methanol solutions but only limited amounts from pure water due to the formation of peroxide intermediates. This is also seen from the non-stoichiometric O_2 evolution from aqueous $AgNO_3$. In methanol, the H_2 evolution rates are inversely correlated with H^+ overpotentials, which shows that the process is limited by the rate of proton reduction on Pt. In water and aqueous silver nitrate, oxygen is inhibited due to the large electrochemical overpotential (2–3 times larger than the H_2 overpotential) that acts as a kinetic barrier for O_2 formation. Instead, peroxide intermediates are favored due to the strong binding affinity of surface peroxides to Nb (5+). The addition of Pt and IrOx cocatalysts do not prevent the formation of niobate-bound peroxides and leads to diminishing hydrogen evolution from water. We also find that cocatalyst attachment causes a depression of the conduction band energy based on the photo-onset potentials. However, this does not affect the activity of the catalysts in the presence of other more important factors.

2.4 Experimental

Reagents: K_2CO_3, Nb_2O_5, and TBA (OH) (40 wt.% in H_2O) were purchased from Acros Organics and used Scheme 2.1. H_2PtCl_{-6} x6H_2O, K_3IrCl_6, H_2SO_4 and HNO_3 (70 %) were purchased from Sigma-Aldrich. KNO_3 and $AgNO_3$ were obtained from Fisher Scientific, Pittsburgh, PA. Reagents were of reagent quality and were used as received. Water was purified to >18 M Ω cm resistivity using a Nanopure system. $K_4Nb_6O_{17}$ was prepared according to a literature method [13].

$(Bu_4N)_4[Nb_6O_{17}]$ scrolls [1]. The scrolls were prepared as described previously [16]. Initially, an acid treatment of 2.0 g (1.93 mmol) bulk $K_4Nb_6O_{17}{\cdot}3H_2O$ powder with 250 mL of 2 M HNO_3 was carried out for 5 days. The resulting white product was centrifuged and washed four times with 50 mL of pure water. Exfoliation of the wet acid exchange product involved adding TBA hydroxide (40 wt.% in water, Acros) in a 20:1 molar ratio (26.6 mL, 40.5 mmol) and stirred for 5 days. This white solution was centrifuged and washed twice with pure water. During the second wash, the precipitate was discarded and the supernatant (containing a homogeneous colloid suspension of nanoscrolls) was isolated for the following study. The concentration of the colloid was measured gravimetrically to be 10 mg/mL which corresponds to an average total of 1.0 g $(Bu_4N)_4$ $[Nb_6O_{17}]$ (28 % yield, M = 1798 g/mol). Transmission electron microscopy (TEM) reveals thin sheets that have rolled into a rod-like structure with multiple layers.

[Pt, IrOx, and Pt/IrOx] $(Bu_4N)_4[Nb_6O_{17}]$ scrolls [2, 3, 4]. Platinum nanoparticles were deposited onto the surface of the niobate scrolls by adding 2.13 mg H_2PtCl_6 (85 wt.% in water, Acros) to a dispersion of 100 mg of niobate scrolls in 50 mL of water. The solution was purged with Ar gas and irradiated under UV-light for 1 h with a Xe-arc lamp. The colored product **3** (Fig. 2.2) was precipitated with 0.1 M H_2SO_4, washed twice with 50 mL of pure water and then re-dispersed in 0.5 wt.% tetrabutyl-ammonium hydroxide in water. Bright field TEM images

reveal the Pt nanoparticles as dark spots (2–3 nm in diameter) containing the characteristic lattice fringes of platinum [19]. Iridium oxide (IrO_x) modified nanoscrolls [**2**] were prepared analogously, using 2.33 mg of K_3IrCl_6 (99.9 % purity, Acros) and 5 mM (25.25 mg) KNO_3 for 100 mg of niobate scrolls dispersed in 50 mL of water. The nitrate is known to facilitate deposition of IrOx [31]. Scanning TEM (STEM) images show additional broader regions of high contrast corresponding to IrO_x deposition. Nanoscrolls containing both 0.5 % Pt and 0.5 % IrOx [**4**] were synthesized in two ways. Pt and IrOx were photodeposited sequentially, with a water washing step (50 mL) after the first deposition. Alternatively, Pt and IrOx were deposited simultaneously using a mixture of 1.17 mg K_3IrCl_6 and 1.07 mg H_2PtCl_6 in 50 mL of 5 mM KNO_3 before washing four times with 50 mL of water. The two products were found to be identical in terms of their morphology and their optical and catalytic properties.

The rate of photochemical hydrogen evolution from each catalyst was determined by irradiating 100 mg of each catalyst in 50 mL of pure water in a quartz round bottom flask with a 300 W Xe-arc lamp (209 mW/cm^2 at flask, $\lambda = 220$–380 nm, measured with GaN photodetector). The air-tight irradiation system connects a vacuum pump and a gas chromatograph (Varian 3800) with the sample flask to quantify the amount of gas evolved, using area counts of the peaks and the identity of the gas from the calibrated carrier times. Prior to irradiation, the flask was evacuated down to 5 torr and purged with argon gas. This cycle was repeated until the chromatogram of the atmosphere above the solution indicated that the sample did not contain hydrogen, oxygen, or nitrogen. Electrochemical measurements were conducted by drying a drop of the aqueous dispersions of the catalyst under nitrogen gas onto a gold electrode (1 cm^2) and submerging the dried product into an air-tight quartz flask filled with 50 mL of 0.25 M Na_2HPO_4/NaH_2PO_4 buffer solution at pH 7, containing 20 % (volume) of methanol as sacrificial donor. The electrochemical cell consisted of a platinum counter electrode, the working electrode (catalyst), and a saturated calomel reference electrode connected to the cell with a KCl salt bridge. Nitrogen gas was bubbled through the electrolyte solution for 10 min prior to each experiment and remained streaming above the solution during the experiment. Photocurrents were measured by irradiation delivered via a fiber optics cable from a 300 W Xe arc lamp equipped with an IR filter. Chopped light with an irradiance of 15 mW/cm^2 at 200–380 nm illuminated the working electrode. The system was calibrated using the redox potential of $K_4[Fe(CN)_6]$ at +0.358 V (NHE). UV/Vis diffuse reflectance spectra were taken on white Teflon tape using an Ocean Optics HR 2000 CG-UVNIR spectrometer and a DH 2000 light source. Centrifugation was achieved with a IEC Centra CL2 centrifuge. Transmission electron images were taken with a Philips CM-12 instrument at 120 kV acceleration potential. Bright field high resolution transmission electron microscopy (BF-HRTEM) images were taken using a JEOL 2500SE 200 kV TEM. Z-contrast high angle annular dark field scanning TEM (HAADF-STEM) images were taken using a JEOL 2100F STEM with 200 kV field emission gun and a spherical aberration corrector.

2.5 Supporting Information

Figures 2.7, 2.8, 2.9, 2.10 and 2.11.

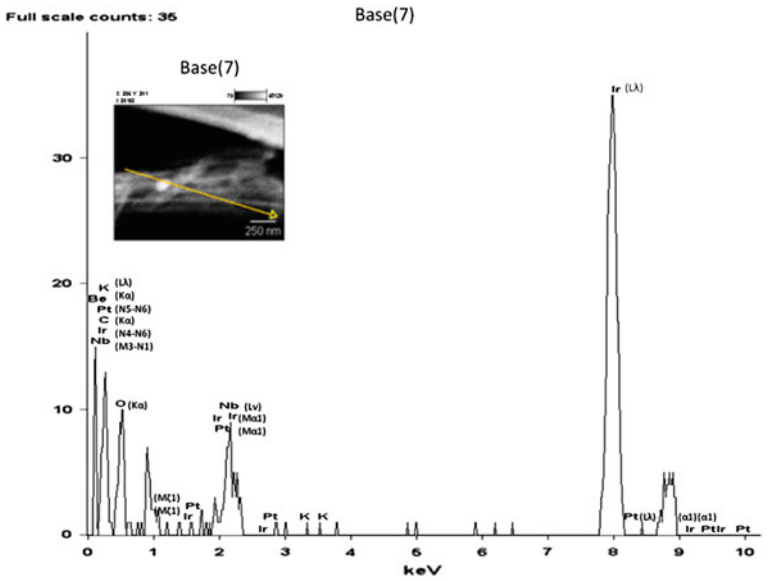


Fig. 2.7 Energy Dispersive X-ray (EDX) line scan spectra of 1:1 Pt/IrO_x-loaded nanoscrolls. The spectra show multiple lines of Pt and Ir indicating their presence directly on the niobate. EDX was performed using a JEOL JEM 2500SE (S)TEM equipped with an EDX system

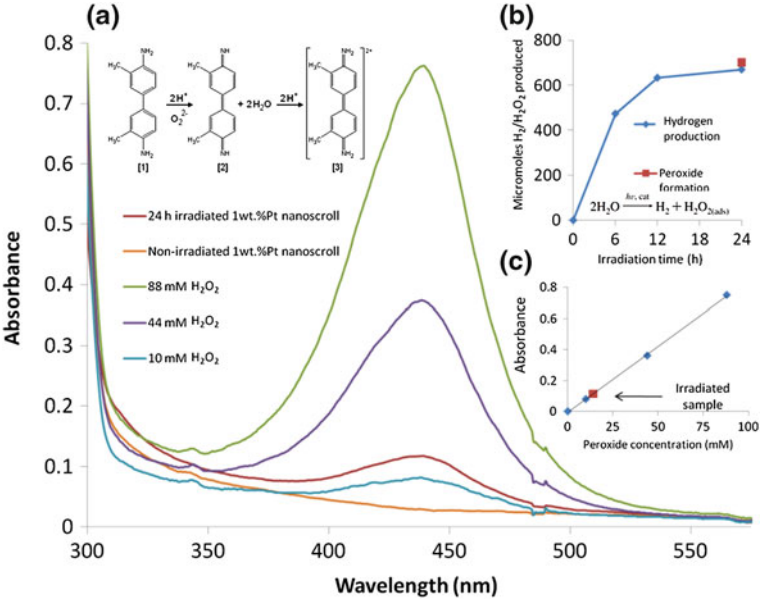


Fig. 2.8 Peroxide determination with o-tolidine. UV-Vis spectra showing absorbance peak at 438 nm of protonated o-tolidine with varying concentrations of hydrogen peroxide plotted with an experimental 24 h water-irradiated nanoscroll sample mixed with o-tolidine. **a** the conversion of o-tolidine from the initial *white* product [1] which reacts with peroxide to form the *blue* product [2] and forms the protonated *yellow* species in acid [3]. **b** time-resolved hydrogen production from 100 mg of 1 wt.% Pt nanoscroll and the corresponding peroxide formation from an aliquot of the catalyst after irradiation. **c** the calibration curve for o-tolidine with hydrogen peroxide standards plotted with the experimental sample. Experiment follows procedure described in [8]

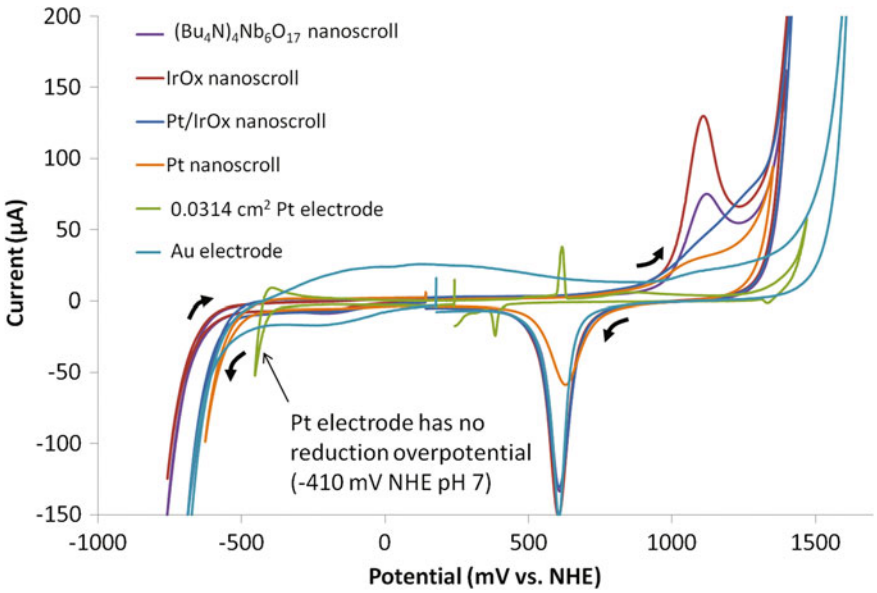


Fig. 2.9 Electrochemical behavior of gold, platinum, and catalyst-coated electrodes. Cyclic voltammetry of four nanoscroll samples deposited as a thin film on a 1 cm^2 gold electrode in 50 mL of pH 7 NaH_2PO_4/Na_2HPO_4 buffer solution with scan rate of 10 mV/s including scans from bare Au electrode and Pt electrode for reference. *Arrows* show scan direction. Both Pt and Au electrodes oxidized water at potentials beyond +1.45 V. This rules out interference with the redox potentials observed for the catalysts, even in regions of partial electrode coverage with catalyst films. As expected, the bare Pt electrode facilitated proton reduction at −410 mV NHE @ pH 7, close to the proton reduction normal potential

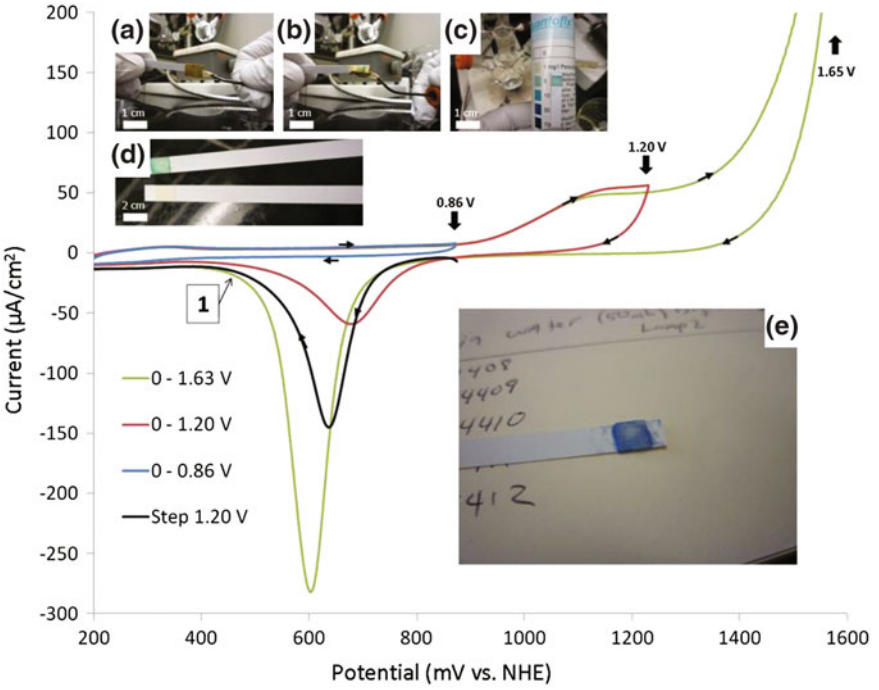


Fig. 2.10 Peroxide detection on gold and niobate-coated electrodes. Cyclic voltammogram of bare gold 1 cm^2 electrode in 0.25 M Na_2HPO_4/NaH_2PO_4 pH 7 buffer with 10 mV/s scan rate. *Arrows* denote scan direction. *Blue*, *red* and *green curves* are components of a three-cycle hysteresis from 0.0 → 0.86 → 0.0 → 1.20 → 0.0 → 1.65 → 0.0 V. The *black curve* from 0.86 → 0.0 V was recorded after a chronoamperometry potential step voltage at 1.2 V for 100 min. Insets **a**–**d** shows qualitative peroxide determination via rubbing a *Quantofix peroxide 100* test strip on the gold electrode surface after 1.2 V chronoamperometry, where **a**–**b** show colored peroxide reaction, **c** approximate peroxide concentration ~3 mg/L, and **d** compares test after 1.2 V potential step (*blue*) and after reduction of peroxides (*white*, no reaction) at 500 mV [point 1]. Similar results were obtained for a film of $(Bu_4N)_4$ Nb_6O_{17} on gold after an electrochemical bias at 1.2 V (NHE) for 1 h (insert **e**)

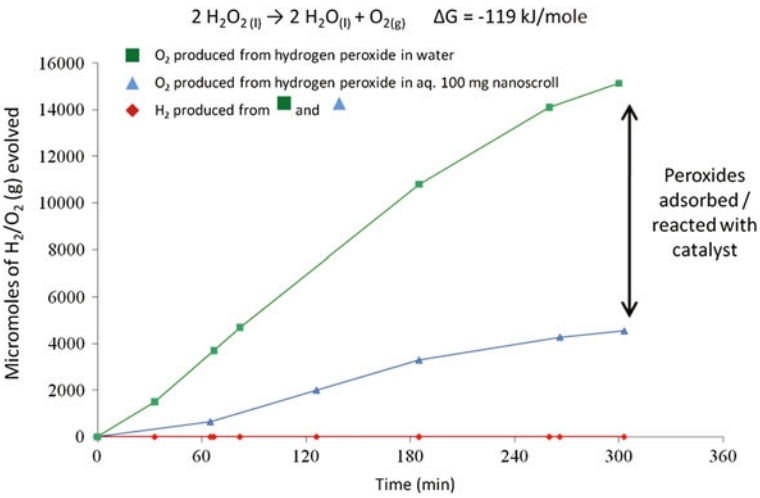


Fig. 2.11 Demonstration of photocatalytic oxygen formation from $(TBA)_4$ Nb_6O_{17} Nanoscrolls (1) in the presence of added H_2O_2. Hydrogen and oxygen evolution during 5 h irradiation of 100 mg aqueous nanoscroll (Δ) with 16 mmol of $H_2O_{2\ (l)}$ (*triangles*) and for pure $H_2O_{2\ (l)}$ solution at identical concentration (*squares*). No hydrogen is evolved in both cases. In the presence of nanoscrolls, only about 25 % of the O_2 is evolved after 5 h, indicating absorption of the added H_2O_2 on the nanoscrolls

Acknowledgments This work was supported by grant 0829142 of the National Science Foundation (NSF) and grant FG02-03ER46057 of the US Department of Energy. T. K. T. thanks NSF for a graduate student fellowship 2010 (NSFGRFP) and his group members for advice. NDB thanks the US Department of Energy for support (Grant FG02-03ER46057).

References

1. N.S. Lewis, D.G. Nocera, P. Natl, Acad. Sci. USA **103**, 15729–15735 (2006)
2. A. Kay, I. Cesar, M. Gratzel, J. Am. Chem. Soc. **128**, 15714–15721 (2006)
3. F.A. Frame, E.C. Carroll, D.S. Larsen, M.S. Sarahan, N.D. Browning, F.E. Osterloh, *Chem. Commun.* 2206–2208 (2008)
4. F.A. Frame, F.E. Osterloh, J. Phys. Chem. C **114**, 10628–10633 (2010)
5. H. Zhou, E.M. Sabio, T.K. Townsend, T. Fan, D. Zhang, F.E. Osterloh, Chem. Mater. **22**, 3362–3368 (2010)
6. E.M. Sabio, M. Chi, N.D. Browning, F.E. Osterloh, Langmuir **26**, 7254–7261 (2010)
7. F.E. Osterloh, in *On Solar Hydrogen and Nanotechnology*, ed. by L. Vayssieres. Nanoparticle-Assembled Catalysts for Photochemical Water Splitting, ch. 16 (Wiley VCH, Weinheim, 2010)
8. O.C. Compton, F.E. Osterloh, J. Phys. Chem. C **113**, 479–485 (2009)
9. M.C. Sarahan, E.C. Carroll, M. Allen, D.S. Larsen, N.D. Browning, F.E. Osterloh, J. Solid State Chem. **181**, 1681–1686 (2008)
10. E.C. Carroll, O.C. Compton, D. Madsen, F.E. Osterloh, D.S. Larsen, J. Phys. Chem. C **112**, 2394–2403 (2008)

11. O.C. Compton, E.C. Carroll, J.Y. Kim, D.S. Larsen, F.E. Osterloh, J. Phys. Chem. C **111**, 14589–14592 (2007)
12. M.R. Allen, A. Thibert, E.M. Sabio, N.D. Browning, D.S. Larsen, F.E. Osterloh, Chem. Mater. **22**, 1220–1228 (2010)
13. M. Gasperin, M.T. Lebihan, J. Solid State Chem. **43**, 346–353 (1982)
14. K. Domen, A. Kudo, M. Shibata, A. Tanaka, K. Maruya, T. Onishi, J. Chem. Soc. Chem. Commun. **23**, 1706–1707 (1986)
15. K. Sayama, A. Tanaka, K. Domen, K. Maruya, T. Onishi, J. Phys. Chem. **95**, 1345–1348 (1991)
16. G.B. Saupe, C.C. Waraksa, H.-N. Kim, Y.J. Han, D.M. Kaschak, D.M. Skinner, T.E. Mallouk, Chem. Mater. **12**, 1556–1562 (2000)
17. R. Kaito, K. Kuroda, M. Ogawa, J. Phys. Chem. B **107**, 4043–4047 (2003)
18. K. Teshima, Y. Niina, K. Yubuta, T. Suzuki, N. Ishizawa, T. Shishido, S. Oishi, Eur. J. Inorg. Chem. **29**, 4687–4692 (2007)
19. B.Y. Xia, J.N. Wang, X.X. Wang, J. Phys. Chem. C **113**, 18115–18120 (2009)
20. M. Yagi, E. Tomita, T. Kuwabara, J. Electroanal. Chem. **579**, 83–88 (2005)
21. F. Mafune, J.Y. Kohno, Y. Takeda, T. Kondow, J. Phys. Chem. B **107**, 4218–4223 (2003)
22. P.G. Hoertz, Y.I. Kim, W.J. Youngblood, T.E. Mallouk, J. Phys. Chem. B **111**, 6845–6856 (2007)
23. G.S. Nahor, P. Hapiot, P. Neta, A. Harriman, J. Phys. Chem. **95**, 616–621 (1991)
24. A. Mills, T. Russell, J. Chem. Soc.-Faraday Trans. **87**, 1245–1250 (1991)
25. I. Burke, P. Nugent, Gold Bull. **30**, 43–47 (1997)
26. D.R. Merrill, I.C. Stefan, D.A. Scherson, J.T. Mortimer, J. Electrochem. Soc. **152**, E212–E221 (2005)
27. P. Vanysek, in *CRC Handbook of Chemistry and Physics*, 88th edn, (Internet Version 2008). (CRC Press/Taylor and Francis, Boca Raton, 2008)
28. A.J. Bard, L.R. Faulkner, *Electrochemical Methods: Fundamentals and Applications* (Wiley, New York, 2001)
29. A. Ishikawa, T. Takata, J.N. Kondo, M. Hara, H. Kobayashi, K. Domen, J. Am. Chem. Soc. **124**, 13547–13553 (2002)
30. K. Akatsuka, G. Takanashi, Y. Ebina, N. Sakai, M. Haga, T. Sasaki, J. Phys. Chem. Solids **69**, 1288–1291 (2008)
31. A. Iwase, H. Kato, A. Kudo, Chem. Lett. **34**, 946–947 (2005)



http://www.springer.com/978-3-319-05241-0

Inorganic Metal Oxide Nanocrystal Photocatalysts for Solar Fuel Generation from Water

Townsend, T.K.

2014, XVI, 71 p. 44 illus., 17 illus. in color., Hardcover
ISBN: 978-3-319-05241-0